EXPERIMENTAL STUDY ON STATIC AND DYNAMIC STABILITY OF A BLUNT BODY CONFIGURATION

Thomas Gawehn and Ali Gülhan

German Aerospace Center (DLR), Institute of Aerodynamics and Flow Technology,
51147 Köln, Germany

ABSTRACT

The aero shape of ESA's Intermediate eXperimental Vehicle (IXV) is prone to suffer from stability problems in the transonic regime. To avoid a supersonic descent system, small fins are implemented to the shape with the aim of passing the transonic flight regime at angles of incidence below $40°$ and improve static stability conditions in subsonic with a lift-to-drag ratio higher than 1.

The fin shape is optimised in a numerical pre-study and two new configurations are investigated experimentally in the Trisonic Wind tunnel TMK of DLR Köln. Static and dynamic aerodynamic coefficients are determined between $Ma = 0.5$ and 2.0 and implemented in an AEDB. The configurations' performance is compared to that of the original IXV aero shape. It can be stated, that implementation of the fins significantly improved the longitudinal static and dynamic stability of the aero shape. The authors therefore recommend further investigations on the new configurations.

Index Terms — Blunt body aerodynamics, static and dynamic stability, wind tunnel testing, IXV aero shape

1. INTRODUCTION

During the atmospheric entry or re-entry of flight vehicles one of the critical issues is the dynamic stability of the vehicle in the transonic regime. This transition phase between supersonic and subsonic flight is known to be particularly hazardous for lifting hypersonic vehicles, whose design is heavily influenced by the need to withstand the harsh environment during hypersonic entry.

During the project activities on ESA's Intermediate eXperimental Vehicle (IXV) it has been revealed that the configuration suffers from transonic static instability at $0° - 40°$ angle of incidence. This has been confirmed in the frame of the DERIVAS study where experiments and simulations were performed to assess the aerodynamic behaviour of the IXV configuration [1, 2].

Beside a static aerodynamic characterization of IXV in the supersonic and transonic Mach range, the free oscillation technique was applied to analyse the dynamic behaviour. Unsteady RANS-simulations using the DLR TAU code were also performed and the results compared with the experiments. An aerodynamic data base was built for the IXV configuration.

The study confirmed the dynamic instability of IXV below a Mach number of $Ma = 1.5$, but also revealed that despite the notable development in numerical tools, the aerodynamic performance of blunt bodies remains difficult to predict by CFD. RANS simulations still have shortcomings, especially at transonic conditions, to capture the flow phenomena in the wake of blunt bodies. LES simulations are more suitable to simulate the flow properties in these cases, but demand much more computational resources and therefore could only be carried out for selected cases.

On the contrary, data of experimental studies suffer under effects of model support arm or sting. Therefore, the test set-up of experimental studies has to be defined carefully and both, experiments and simulations, need to be used in a complementary way.

With regard to IXV, one option for improving the dynamic stability is changing its external shape slightly e.g. by adding small fins. Such modifications could improve static and dynamic stability behaviour of the vehicle and decrease the angle of incidence and thereby increase lift-to-drag ratio. This modification should improve flying qualities of the vehicle in the critical transonic regime and avoid the implementation of supersonic descent systems.

Therefore, the actual study is performed on two modified IXV aero shapes whereby the fin geometry was optimised in a numerical pre-study with the FOI EDGE code [3]. Static and dynamic wind tunnel tests are performed in the TMK wind tunnel in a wide Mach range (0.5 to 2.0) and compared to the aerodynamic data of the original IXV configuration. Numerical simulations using the DLR TAU code [4] and the FOI EDGE code [5] are performed at selected test points, but results will not be presented herein. Combining the different tools helps in understanding the acting flow phenomena and thereby in improving the simulation techniques. Besides, the results allow for an evaluation of the suitability of the fins to be applied to a future mission of IXV.

2. EXPERIMENTAL SETUP

2.1. Trisonic Wind Tunnel Köln (TMK)

TMK is a trisonic blow down wind tunnel with a rectangular test section of $0.6\,m\,x\,0.6\,m$ that is equipped with large quartz glass windows on opposing sides. As sketched in Figure 1, air from a pressure reservoir passes a storage heater and a settling chamber and is then accelerated in an adaptable Laval nozzle. In the test section, flow conditions are nearly constant before the flow is decelerated downstream in the diffuser system. Depending on Mach and Reynolds number a maximum testing time of up to 60 seconds is achieved.

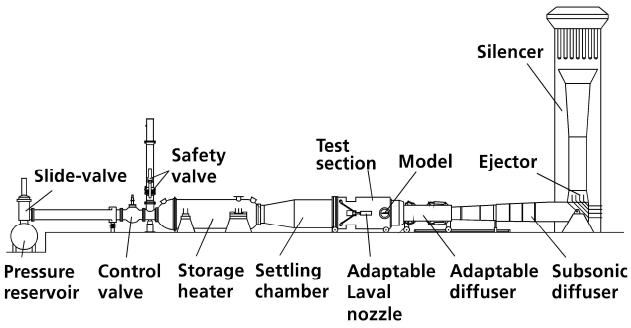

Figure 1: Schematic of Trisonic Wind Tunnel.

The performance map of the facility is given in Figure 2. Standard Mach number range is $1.25 < Ma < 4.5$ where the wind tunnel is operated at a dynamic pressure of $q_\infty \approx 1\,bar$. Mach number is controlled by the adaptable Laval nozzle while the diffuser is usually fully open. Tests with reduced dynamic pressure or Mach numbers up to $Ma = 5.7$ can be realised by ejecting additional air mass flow downstream of the subsonic diffuser and, if necessary, heating the flow in the storage heater.

For Mach numbers of $0.5 < Ma < 1.2$ an additional transonic test section with perforated walls of variable aperture is installed downstream of the supersonic test section. Then, the wind tunnel is operated at a static pressure of $p_\infty \approx 1\,bar$ and the Mach number is controlled via the adaptable diffuser downstream of the test section.

Facility instrumentation and calibration

The stagnation conditions T_0 and p_0 are measured in the settling chamber of TMK with a type K thermocouple of tolerance class 1 (accuracy of $\pm 1.5\,K$) and a PMP 4015 pressure sensor of GE Sensing with a given accuracy of ± 0.04 % full scale. Depending on the test condition, a sensor of 3, 10 or 30 bar range is used.

From supersonic calibration data of the adaptable Laval nozzle the Mach number in the centreline region of the wind tunnel is known to differ less than ± 0.5 % of the nominal value for $Ma \geq 2.0$. With decreasing Mach number, the relative error increases slightly to ± 0.75 % at $Ma = 1.5$ [6].

For transonic tests the Mach number and its uncertainty is calculated from the pressure ratio p_0/p_∞ using gas dynamic equations and applying correction factors derived from calibration tests. Thereby, the static pressure p_∞ in the test section is measured relative to the atmosphere with a Pm131TC differential sensor of $0.7\,bar$ range and $\pm 0.0017\,bar$ total uncertainty.

Via the model support system, the angle of incidence can be varied continuously during a test while the incidence angle α is measured by an angle transmitter with an accuracy of better than $\pm 0.05°$. Additionally, from calibration data, the flow angularity in vertical and horizontal planes $\Delta\alpha$ and $\Delta\beta$ are known to be less than $\pm 0.25°$ whereby this value could increase towards the operating limits of the wind tunnel [6].

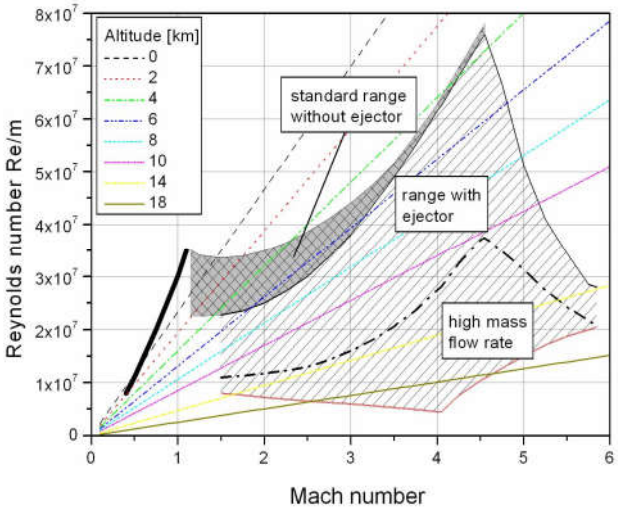

Figure 2: Performance map of Trisonic Wind Tunnel.

2.2. Wind tunnel models

The IXV aero shape is used as baseline geometry. To overcome the unstable aerodynamic behaviour in the transonic flight regime, short fins are integrated at the rear part of the vehicle (Figure 3). Within a numerical study, shape and position of the wings are optimised [3]. Aim of the shape modification is the extension of the stable flight regime down to transonic range below $Ma = 1.5$, a lift-to-drag ratio of $L/D > 1$ and a trimmed incidence angle of $\alpha_{trim} < 30°$ for $Ma \leq 1$. This higher L/D will offer the possibility to reach pilot chute release at $Ma = 0.8$ or below and altitude close to $10\,km$ or even lower, for a mission sequence based on a subsonic parachute.

The model scale is defined to $1:35.2$, i.e. the model reference length is $L_{Ref} = 0.125\,m$ (without flaps) and the reference surface is $S_{Ref} = 0.0058594\,m^2$. The Moment

Reference Centre (MRC) is defined as for the IXV-vehicle: $x_{MRC} = 0.0725\ m$, $y_{MRC} = 0.0\ m$, $z_{MRC} = -0.003125\ m$.

Two types of fin shape are investigated, one aerodynamically optimised geometry based on a NACA profile and a simplified geometry base on a rectangular shape. As the difference in aerodynamics is minor, only results for the easier to manufacture rectangular shaped version, named "Dynast_r", are presented hereafter.

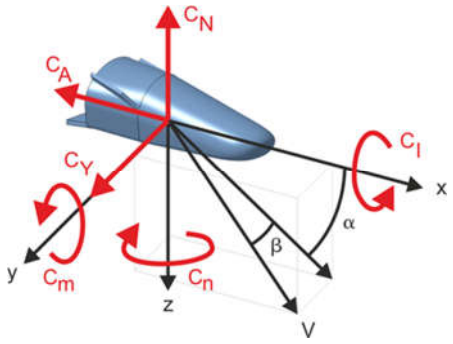

Figure 3: Dynast_r (IXV with integrated fins).

Model A for static tests

The model design for static tests in Figure 4 shows the wind tunnel model fitted on a six component strain gauge TASK® balance. Balance axis and model axis are inclined by 2°. The fin section is exchangeable allowing for tests with different fin geometries and, for cross-checking purposes, also without fins (IXV aero shape). The design includes three different sets of flaps with $\delta_f = \pm 5°$ and 0° deflection angle. The setup is used to investigate the static aerodynamic behaviour of the defined aero shapes.

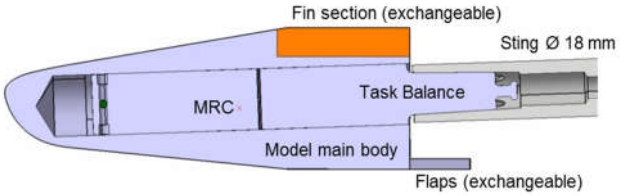

Figure 4: CAD view of static wind tunnel model A.

Model B for dynamic tests

The key element of model B for dynamic tests is an elastic cross-flexure. It provides the necessary motion around the Centre of Rotation (CoR) which is designed to be as close as possible to the model's Centre of Gravity (CoG) (Figure 5). The model's moment of inertia I_y and the stiffness of the cross-flexure c_y determine the reduced frequency parameter within wind tunnel testing. As several constraints related to model and support design and related to the loads acting on the model during tests have to be taken into account, design of both parameters (I_y and c_y) aims to be a compromise for the Mach number range to be investigated. Thereby, the complete setup should allow for about 20 oscillation cycles at 3 different releases during one wind tunnel test.

A cross-flexure with a stiffness of $c_y = 4\ Nm/rad$ is used and a deflection limiter implemented within the release mechanism to protect the cross-flexure from overload. Deflection of model and cross-flexure is limited to $-2° \leq \theta_{defl} \leq +2°$.

Cross-flexure's stresses are checked against material properties analytically and via the FEM-tool ANSYS R16.0. The results confirm operability of the system at all desired dynamic test points as long as the offset of the centre of pressure to the centre of rotation is below $0.4\ mm$. Otherwise, the model would not oscillate and hit a deflection limiter.

Instrumentation of the cross-flexure consists of special strain gauges (German: Dehnungsmessstreifen DMS) that are connected in Wheatstone full-bridge circuits. The measured DMS-voltage signals correspond to the deflection angle θ_{defl} of the cross-flexure.

Figure 5 shows the mechanism used for free oscillation tests. It consists of cross-flexure, adapter, stepper motor, gearing and release mechanism. Sting and model axis are inclined by 5° to realise the CoR in the MRC of the model. Trim weights are integrated to achieve CoG≈MRC. An exchangeable rear part of the model allows for investigations with different fin sections and the IXV-geometry. Based on the test matrix for dynamic tests, 10 sets of flaps are manufactured between $\delta_f = 0°$ and $+5.5°$.

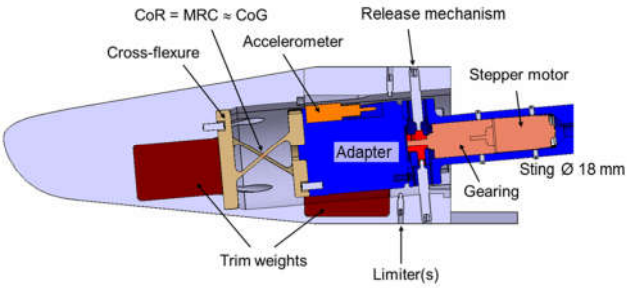

Figure 5: CAD view of dynamic wind tunnel model B.

3. MEASUREMENT TECHNIQUE

3.1. Static aerodynamic measurements

Aerodynamic coefficients (for definition see Figure 3) are determined via the 6 −component TASK balance inside of the wind tunnel model. Before the test campaign, calibration of the balance is performed in a special test stand. The calibration is cross-checked after installation of the balance into the wind tunnel.

To reduce normal forces on the balance, the model is aligned at low angle of incidence at wind tunnel start-up until the test condition is reached. Then, continuous alteration of the angle of incidence allows for acquisition of aerodynamic data along the complete polar. The wind tunnel

is shut-down with the model again at low angle of incidence.

During static tests, data of the balance and all sensors are recorded simultaneously with an acquisition rate of $100\ Hz$ and stored together with all calibration information. Post-processing is performed after the test handling the data with an in-house tool.

3.2. Determination of derivatives

The applied method analyses free oscillations of the scaled wind tunnel model with and without flow influence. Therefore, the model is fixed to a sting by means of a cross-flexure and oscillates with one degree of freedom around its centre of gravity. As the pitch rate q is equal to the derivative $\dot{\alpha} = \dot{\theta}$, it cannot be distinguished between the two derivatives C_{mq} and $C_{m\dot{\alpha}}$. Only the sum of both can be determined.

The motion of the model is considered as a small deflection relative to the trimmed position (θ_{trim}) that is described by the following differential equation:

$$I_y\ddot{\theta} + \left(k_y - M_{\dot{\theta}}\right)\dot{\theta} + \left(c_y - M_{\theta}\right)\theta = 0 \qquad (1)$$

with I_y the moment of inertia, k_y the mechanical damping, c_y the mechanical stiffness, $M_{\dot{\theta}}$ the aerodynamic damping and M_{θ} the aerodynamic stiffness.

Using the common ansatz for a damped harmonic oscillation

$$\theta(t) = \theta_{defl}\, e^{-\delta t} e^{i\omega t} \qquad (2)$$

with θ_{defl} the oscillation amplitude, δ the damping decrement and ω the angular frequency, the aerodynamic stiffness and damping coefficients can be calculated as:

$$M_{\theta} = -I_y(\omega^2 + \delta^2) + c_y \;\rightarrow \qquad (3)$$

$$C_{m\alpha} = \frac{M_{\theta}}{\frac{\rho_{\infty}}{2} u_{\infty}^2 S_{Ref} L_{Ref}}, \qquad (4)$$

$$M_{\dot{\theta}} = -2I_y\delta + k_y \;\rightarrow \qquad (5)$$

$$\left(C_{mq} + C_{m\dot{\alpha}}\right) = \frac{M_{\dot{\theta}} \cdot u_{\infty}}{\frac{\rho_{\infty}}{2} u_{\infty}^2 S_{Ref} L_{Ref}^2}. \qquad (6)$$

k_y is the mechanical damping and $c_y = f(F_{ax})$ the mechanical stiffness which is a function of the axial load on the cross-flexure. This relation is known from calibration of the system. ρ_{∞} and u_{∞} represent the density and velocity of the free stream, S_{ref} and L_{ref} are model reference parameters.

A more elaborate description on the free oscillation technique, cross-flexure calibration and the procedure to derive dynamic derivatives from the measured oscillations can be found in [1].

3.3. Flow visualization

Schlieren visualization in TMK uses a Z-arrangement and a simultaneous recording on two camera systems:

1. a monochromatic PHOTRON Fastcam ultima APX-RS (Frame rate: up to 150 kHz, min. exp. time: 1 µs, sensor: CMOS, res.: 1024x1024 px, bit depth: 10 bit) and
2. a monochromatic PROSILICA GE4000 (Frame rate: up to 5 Hz, min. exp. time: 140 µs, sensor: CCD, res.: 4008x2672 px, bit depth: 16 bit).

Application of the oil film technique allows for visualization of near surface streamlines. Therefore, the model surface is prepared with a thin layer of a special mixture (oil, petroleum, fluorescent pigments) that dries during the test while flow conditions and incidence angle are kept constant. The formed pattern characterizes the average shear forces on the model surface and is photographed after the test.

4. EXPERIMENTAL ANALYSIS

Static tests are performed with model A to determine the aerodynamic behaviour of the Dynast configurations in comparison to the original IXV. The investigated Mach number thereby ranges from $Ma = 0.5$ to 1.1 in the transonic tests section of TMK and from $Ma = 1.3$ to 2.0 in the supersonic test section. Schlieren images could only be recorded for supersonic tests, but oil flow visualisation is performed at selected transonic test conditions.

Dynamic tests with model B using the free oscillation technique could only be performed near the trim condition which is at each Mach number an individual combination of flap deflection angle δ_f and model incidence angle α. As statically stable trim points of the original IXV shape only exist for incidence angles $\alpha \geq 40°$, dynamic tests with the actual setup (sting at the base) could only be performed with both Dynast configurations. Schlieren videos are recorded during supersonic dynamic tests.

4.1. Static aerodynamic measurements

During one test, flow conditions are kept constant, but the angle of incidence is varied continuously with $3°/s$ in the range of $-2° \leq \alpha \leq +35°$ (for transonic tests) and $-2° \leq \alpha \leq +44°$ (for supersonic tests). Tests are performed with a flap deflection angle of $\delta_f = -5°$, 0° or +5°.

In the following figures, the axial force (C_A), normal force (C_N), pitching moment (C_m) and negative base pressure coefficient ($-C_{pB} = -[p_B - p_{\infty}]/q_{\infty}$), calculated from tests at four different Mach numbers, are shown for Dynast_r (solid lines) and the reference configuration IXV (dashed lines), both with a flap deflection of $\delta_f = 0°$.

From the plots it can be observed, that the fins have only minor influence on the axial force coefficient, except at $Ma = 0.6$ and angle of incidence $\alpha \geq 20°$ (Figure 6) where C_A is lower with fins. Minor discontinuities at $Ma = 0.6$

above $\alpha \approx 25°$ are observed for both configurations which implies that they are caused by flow phenomena acting on the identical main body.

As the measured C_A values are plotted without applying any corrections, the corresponding base pressure data are given in Figure 7. It can be seen that the base pressure coefficients are comparable for both configurations up to an angle of incidence of $\alpha \approx 20°$.

Figure 8 shows the normal force coefficients. As expected, the fins slightly increase the coefficient at all Mach numbers. For $Ma = 0.95$ and $Ma = 1.1$ a clear change in the gradient of C_N is visible as the angle of incidence increases above $\alpha \approx 25°$. At $Ma = 1.5$ this change is less distinct and reversed above $\alpha \approx 30°$.

The pitching moment distribution for Dynast_r and IXV is shown in Figure 9. Obviously, this coefficient is highly influenced by integration of the fins. While IXV shows a statically instable behaviour at $Ma = 0.6$ for the complete investigated α-range, the gradient of $C_{m\alpha}$ is about zero around $\alpha \approx 20°$ for Dynast_r and even negative for higher angle of incidence. In combination with a positive flap deflection, this would allow for a statically stable trim

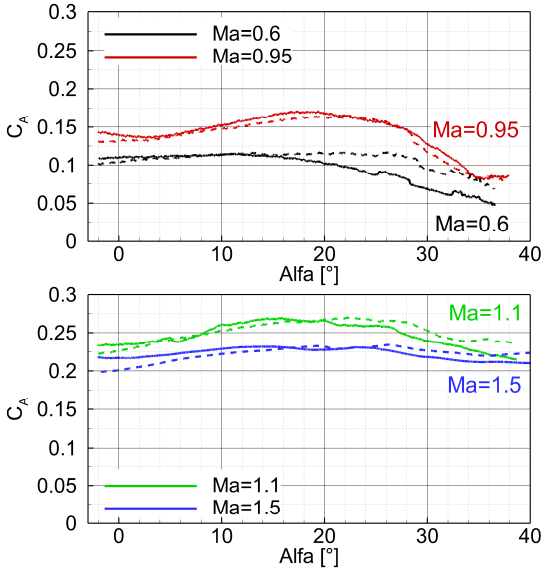

Figure 6: Axial force coefficient (C_A) of Dynast_r (solid) and IXV (dashed), $Ma = 0.6, 0.95, 1.1, 1.5, \delta_f = 0°$.

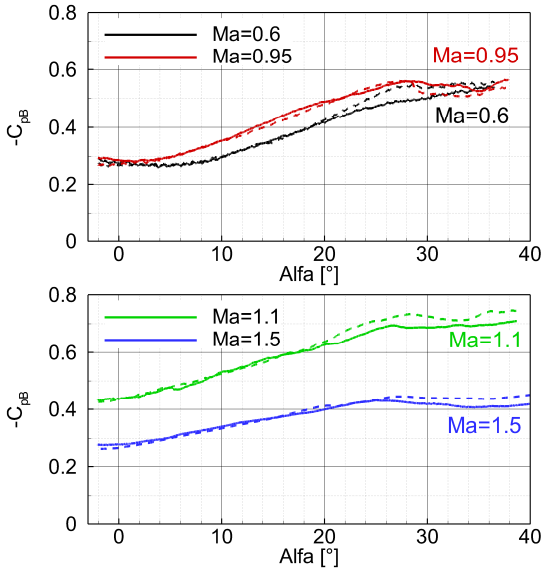

Figure 7: Base pres. coeff. ($-C_{pB}$) of Dynast_r (solid) and IXV (dashed), $Ma = 0.6, 0.95, 1.1, 1.5, \delta_f = 0°$.

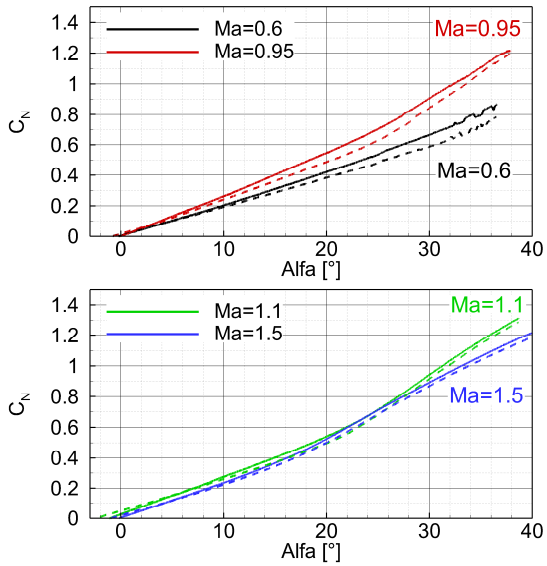

Figure 8: Normal force coeff. (C_N) of Dynast_r (solid) and IXV (dashed), $Ma = 0.6, 0.95, 1.1, 1.5, \delta_f = 0°$.

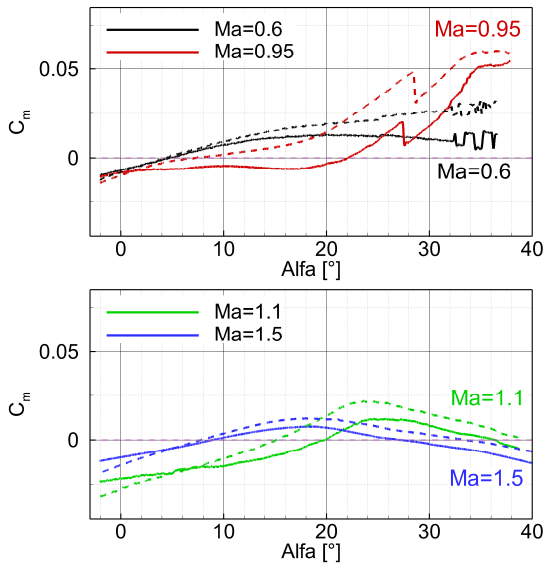

Figure 9: Pitching mom. coeff. (C_m) of Dynast_r (solid) and IXV (dashed), $Ma = 0.6, 0.95, 1.1, 1.5, \delta_f = 0°$.

condition at $Ma = 0.6$ in the range of $20° \leq \alpha \leq 30°$. Higher angles of incidence should be avoided as instationary effects seem to occur beyond $\alpha \approx 32°$.

$Ma = 0.95$ proves to be a difficult condition with respect to static stability. Although, static stability could not be fully achieved by implementation of the fins, Dynast_r provides lower values for C_m and a gradient $C_{m\alpha}$ that is significantly decreased, at least for angels of incidence below $\alpha \approx 22°$, in comparison to IXV. However, both configurations possess a discontinuity on the C_m slope at $\alpha \approx 28°$. It is assumed that this is caused by the onset of flow separation on the leeward side of the vehicle, but could not be proved within the experimental test campaign.

At supersonic conditions, statically stable trim points can be found for IXV and Dynast_r with $\delta_f = 0°$, but with fins the trim angle is about 2° lower at $Ma = 1.1$ and about 6° lower at $Ma = 1.5$. This reduction in trim angle directly affects the performance of the configuration at trim condition with respect to an increased L/D ratio [3].

4.2. Dynamic stability tests

From the performed static experiments with different flap deflection angles ($\delta_f = 0°; \pm 5°$) linear interpolation for data at one Mach number leads to potential trim conditions with $C_m = 0$, i.e. combination of Mach number Ma, flap deflection angle δ_f and angle of incidence α. Preferably, a trim point with the gradient $C_{m\alpha} = \partial C_m / \partial \alpha < 0$ is chosen, where the configuration is statically stable.

For $Ma > 1$, statically stable trim conditions can be found with $\delta_f = 0°$ and, therefore, dynamic tests are performed at these points. In contrary, at Mach numbers $Ma < 1$ static stability is not achieved at all Mach numbers. Then, a small positive gradient $C_{m\alpha} > 0$ is accepted that will be compensated by the cross-flexure for dynamic tests and by flap activation during flight.

Within a dynamic wind tunnel test, the sting angle, taking into account the pretended bending of the sting due to the acting aerodynamic forces, is set prior to wind tunnel start up. The cross-flexure is blocked until the test condition is set. Then, the model is deflected and released several times using the implemented mechanism. Wind tunnel data, sting bending (instrumented with DMS near sting root) and the oscillation of the model measured via the DMS signals of the cross-flexure, are recorded with a frequency of 4 kHz. Finally, cross-flexure is blocked again and the wind tunnel shut down.

Figure 10 shows a schlieren image of a dynamic test with Dynast_r at $Ma = 2.0, \delta_f = 0°, \alpha_{trim} = 37.2°$ at decayed model oscillation. Silhouettes of the model in red and green indicate the initial deflection range of $\Delta\theta = \pm 2°$. The CoR (cross-flexure axis) is also marked in the image.

The recorded signal of the cross-flexure is used to calculate the incidence angle over time given by the blue line in Figure 11. Applying the ansatz for a damped har

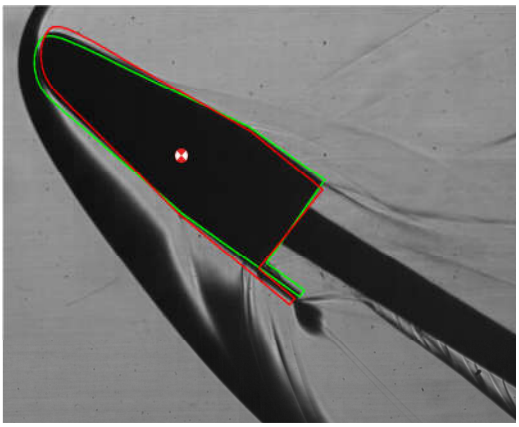

Figure 10: Schlieren image of dynamic test with Dynast_r, $\Delta\theta = \pm 2°, Ma = 2.0, \delta_f = 0°, \alpha_{trim} = 37.2°$.

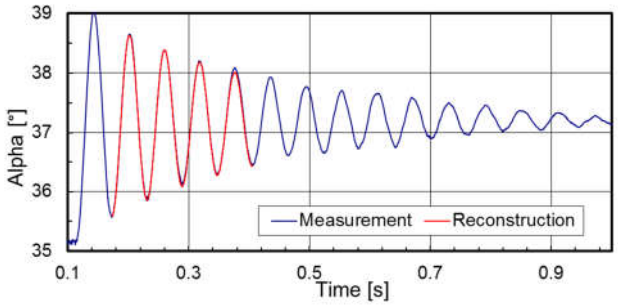

Figure 11: Recorded model oscillation (blue), reconstructed signal (red), $Ma = 2.0, \delta_f = 0°, \alpha_{trim} = 37.2°$.

monic oscillation in equation (2), the signal is reconstructed starting one period after the release (red line). Thereby, the relevant oscillation parameters (damping δ and angular frequency ω) are determined and used for calculation of the dynamic derivatives with equations (3) and (4).

As the model is released several times during one test and most tests are also repeated, a number of 2 to 8 releases is used to calculate the dynamic derivatives. The aerodynamic stiffness $C_{m\alpha}$ for each release, together with mean values and uncertainty margins, is plotted against Mach number in Figure 12. The trim angle α_{trim} and the flap deflection angle δ_f are also given in the figure.

The dynamic tests confirm the observations from static tests, that the Dynast_r configuration is statically stable at all supersonic conditions. $C_{m\alpha}$ is just negative at Ma=1.1 with $\alpha_{trim} = 30.2°$ and $\delta_f = 3.5°$, but static stability margin increases with Mach number as also the trim angle does. At $Ma = 2.0$ the trim angle is already $\alpha_{trim} = 37.2°$. All supersonic tests with $Ma \geq 1.3$ are performed with $\delta_f = 0°$.

In transonic, the trim angle is only around $\alpha_{trim} = 22°$, but the vehicle gets slightly statically instable in the range $0.9 \geq Ma \geq 0.6$. Flap deflection ranges from $\delta_f = 1°$ at $Ma = 0.9$ to $\delta_f = 5°$ at $Ma = 0.6$. Below, static stability is found again ($Ma = 0.5$, $\alpha_{trim} = 26.6°$, $\delta_f = 3.5°$).

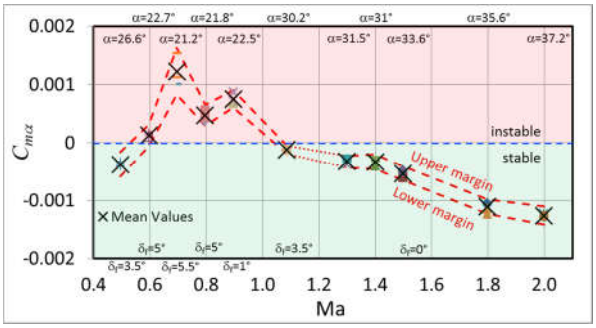

Figure 12: $C_{m\alpha}$ of Dynast_r configuration.

The pitch damping sum $(C_{mq} + C_{m\dot{\alpha}})$ of each release is plotted on Mach number in Figure 13 together with mean values and uncertainty margins. Repeated releases of the model in one run could lead to a slightly different oscillation of the model and thus to a small difference in the determined derivatives. Thereby, spreading of the individual values around the average is relatively low at supersonic test conditions. Same accounts for tests at $Ma = 1.1, 0.8, 0.5$ in the transonic test section. The highest deviations and uncertainties are observed at $Ma = 0.9$ and $Ma = 0.7$.

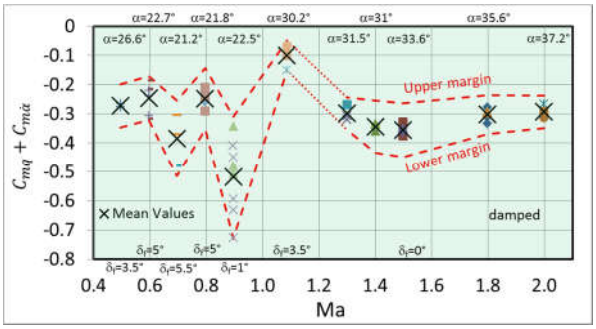

Figure 13: $(C_{mq} + C_{m\dot{\alpha}})$ of Dynast_r configuration.

The pitch damping sum is negative throughout the complete investigated Mach number range. In combination with $C_{m\alpha} < 0$ this gives **static and dynamic stability** of the Dynast_r configuration at the corresponding test conditions, i.e. at $Ma = 0.5$ and for $Ma \geq 1.1$, all with a trim angle of $\alpha_{trim} \leq 40°$ and a flap deflection of $\delta_f \leq 3.5°$.

At statically indifferent or instable conditions, for $0.9 \geq Ma \geq 0.6$, the negative pitch damping sum leads to slower dynamics for the transition of the vehicle to a stable point making the system simpler to control. Positive derivatives in contrast would lead to a system that is stiffer to control and may result in an oversized GNC system.

4.3. Flow visualization

Density gradients

Schlieren images at $Ma = 1.5$ are shown in Figure 14, on top for an incidence angle of $\alpha = 25.1°$ and below for $\alpha = 33.6°$, the trim angle at that Mach number. The bow shock ahead of the vehicle is clearly visible in both images, but also weaker shock waves and expansion lines. The main flow features are marked with characters to better show their correspondence in the two images. Additionally, the shadows of the two base pressure pipes are visible. Unfortunately, in the used schlieren setup, not only shock waves but also strong expansion regions appear in dark.

First observation is, that at $\alpha = 25.1°$, the leeward flow stays attached to the surface whereas at $\alpha = 33.6°$ it separates downstream of the nose (l), reattaches (m) and again separates (n). The separated flow together with the higher incidence angle changes slightly the leeward shock waves (a, b and c). Downstream of the model, the strong shock wave (e) attaches to the sting at $\alpha = 25.1°$, but stays detached at $\alpha = 33.6°$ and shock wave (d) nearly vanishes at the higher angle of incidence.

On the windward side, the change in incidence angle not only changes the shock angles, but also their structure and strength. The expansion line (f) occurs in both images as does also shock wave (i), but shock wave (g) at $\alpha = 25.1°$ is shifted significantly downstream for $\alpha = 33.6°$ and splits into two branches. A new shock (k) occurs between these branches and the expansion line (f).

At $\alpha = 25.1°$ a Mach line is visible at the flap's leading edge although the step height is below $0.1\ mm$ (h). This is not the case at the higher incidence angle. At the flaps trailing edge, the expansion is visible in dark in both images. It increases with angle of incidence and the emanating shock wave (j) gets steeper and hits the sting more upstream.

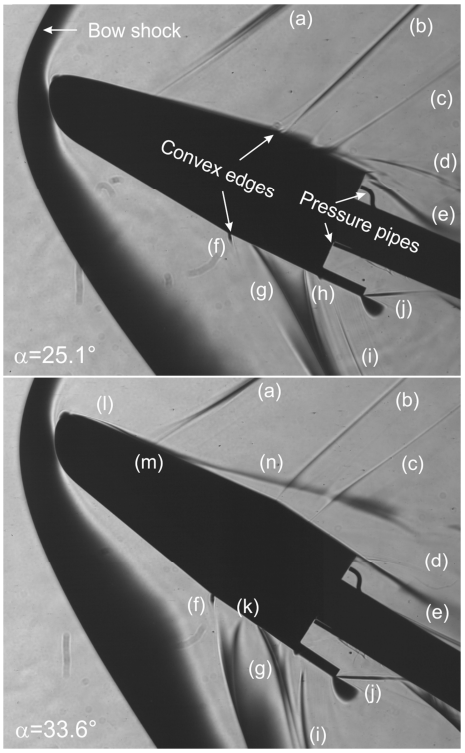

Figure 14: Schlieren images at Ma=1.5, δ_f =0°.

Surface streamlines

Due to perforated sidewalls in the transonic test section, the flow field is not accessible by optical means during the tests. Therefore, the oil film technique is applied at all trim conditions in the range $0.5 \leq Ma \leq 1.1$ to at least visualize the average near surface streamlines.

Figure 15 shows oil flow images of the leeward (top) and the left side (bottom) of the Dynast_r configuration, photographed after a test at $Ma = 1.1$ ($\delta_f = 3.5°$, $\alpha_{trim} = 30.2°$). Analysing the structures, a significant leeward flow separation at the nose with reattachment is visible. The downstream pattern is likely to represent two vortices, one on each side, before flow constriction leads to a "jellyfish-like" structure. Further downstream another vortex pair is visible causing relatively high shear forces along the fins, but relatively low forces in the central body region.

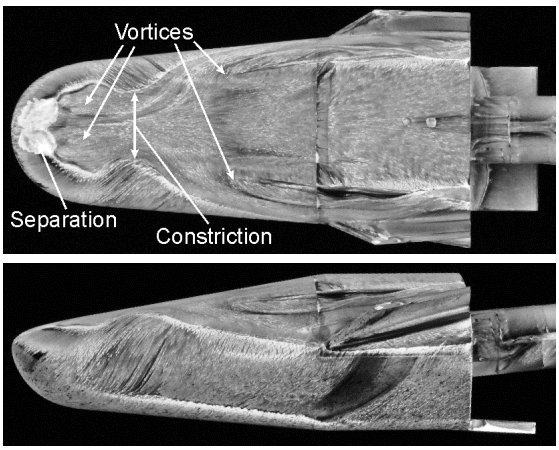

Figure 15: Oil flow visualization, leeward and side view, $Ma = 1.1, \delta_f = 3.5°, \alpha_{trim} = 30.2°$.

The oil flow pattern on the vehicle's side shows that the flow sweeps far around the vehicle's nose causing the constriction visible on the leeward side. At the rear part, a large oil-free area is visible. It is assumed that vortices emanate from the model corners upstream and wrap around the model's tail causing lateral shear forces and oil transportation. This could lead to the observed flow structure. As the effort to produce oil flow visualization at one single test point is relatively high, this technique is not applied to supersonic test conditions.

5. CONCLUSION

Within an experimental study in TMK wind tunnel, the static and dynamic aerodynamic coefficients of the finned Dynast_r configuration have been determined and compared to data of the finless IXV. The obtained data show that implementation of the fins decreases the trim angle in supersonic and thereby increases the L/D ratio. In subsonic, the static stability is significantly increased even enabling to find stable trim conditions for $Ma \leq 0.6$. Dynast_r proved to be either statically stable, indifferent or only slightly instable throughout the complete investigated Mach number range ($0.5 \leq Ma \leq 2.0$). Dynamically, damped oscillations were recorded for all test conditions. These observations are confirmed by numerical studies performed on the Dynast_r configuration using the DLR TAU code [4] and the FOI EDGE code [5].

Static and dynamic coefficients of both Dynast configurations were implemented in AErodynamic DataBases (AEDBs) and provided for a Flight Performance Analysis [7]. As outcome, both finned configurations prove to be promising in decreasing the trim angle and thereby increasing the L/D-ratio.

As conclusion of the actual study, the modified aero shape seems to successfully overcome the stability issues of IXV in the transonic range. Nevertheless, in order to achieve a deeper understanding of the configuration capabilities and performance, a fine tuning of the vehicle's centre of gravity, as well as the extension of the aerodynamic database to lateral-directional plane and to wider elevator deflection are recommended.

6. REFERENCES

[1] Gülhan, A.; Klevanski, J.; Gawehn, T.; *Experimental study on the dynamic stability of the IXV configuration*. 8th European Symposium on Aerothermodynamics for Space Vehicles, Lisbon, Portugal, March 2-6, 2015.

[2] Reimann, B.; *Numerical Prediction of Longitudinal Dynamic Stability for a Lifting Body in Transonic Flow*. 34th AIAA Applied Aerodynamics Conference, Washington, D.C., USA, 13-17 June, 2016, AIAA2016-3578.

[3] Gawehn, T.; Reimann, B.; Tysell, L.; Bonetti, D.; Jirasek, A.; Johnstone, E.; Clopeau, E.; Gülhan, A.; Ferracina, L.; Molina, R.; *Experimental and numerical investigation on the dynamic stability of a blunt body configuration*. FAR conference, Monopoli, Italy, 30 September - 3 October, 2019.

[4] Reimann, B.; Gawehn, T.; *Numerical Investigation of Wind Tunnel Test to Measure Dynamic Stability*. FAR conference, Monopoli, Italy, 30 September - 3 October, 2019.

[5] Tysell, L.; Dalenbring, M.; *Hybrid RANS/LES computations of pitch damping derivatives for a blunt body configuration*. FAR conference, Monopoli, Italy, 30 September - 3 October, 2019.

[6] Esch, H.; *Die 0.6-m x 0.6-m-Trisonische Meßstrecke (TMK) der DFVLR in Köln-Porz (Stand 1986).* Mitteilung, DRVLR-Mitt. 86-21, DFVLR, Hauptabteilung Windkanäle, Köln, 1986.

[7] Bonetti, D.; Medici, G.; Arnao, G. B.; Riley, D.; *Flying Qualities Analysis Of Dynast (Dynamic Stability Of Capsules And Blunt Bodies At Angle Of Attack)*. FAR conference, Monopoli, Italy, 30 September - 3 October, 2019.

7. ACKNOWLEDGMENTS

This work was performed in the framework of the Technology Research Program of the European Space Agency under Contract No. AO/1-8023/14/NL/SW. The authors would like to thank ESA for the support of this project.